Joule

CellPress
OPEN ACCESS

Article

Upper efficiency limit of Sb_2Se_3 solar cells

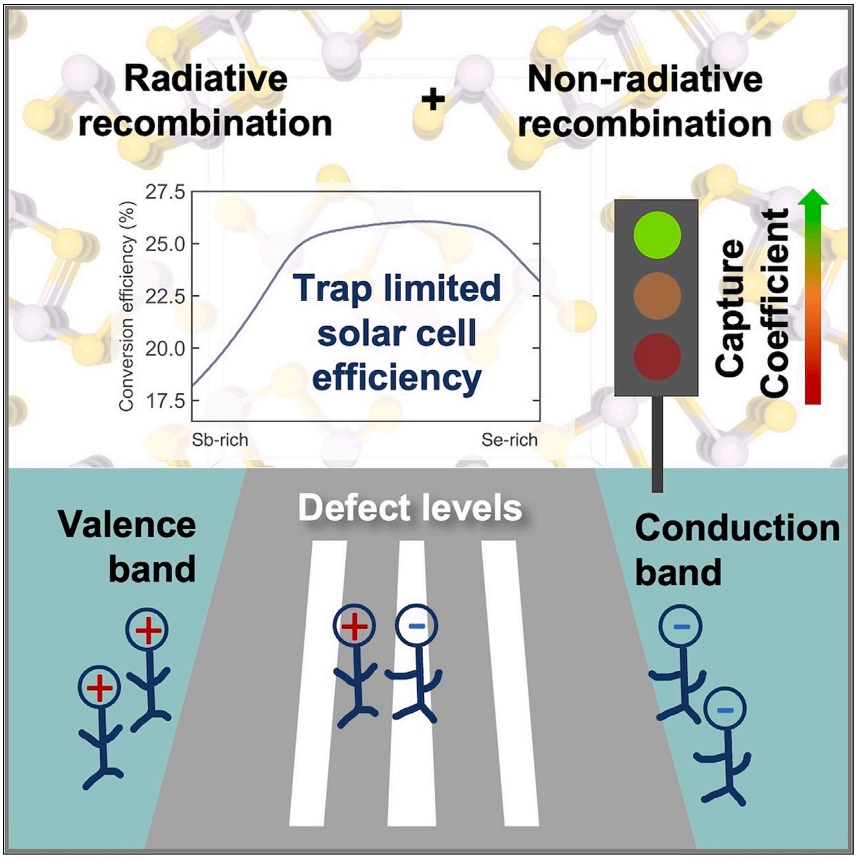

The record light-to-electricity conversion efficiency of antimony selenide solar cells is 10%. First-principles analysis predicts that the material can achieve much higher performance once the most harmful point defects are avoided.

Xinwei Wang, Seán R. Kavanagh, David O. Scanlon, Aron Walsh

a.walsh@imperial.ac.uk

Highlights

Set an upper limit of 26% efficiency for Sb_2Se_3 solar cells from first principles

Predict optimal growth conditions that minimize detrimental defects

Identify vacancies as responsible for the open-circuit voltage deficit

Suggest further improvements by controlled exposure to oxygen

Wang et al., Joule 8, 2105–2122
July 17, 2024
https://doi.org/10.1016/j.joule.2024.05.004

Joule

CellPress
OPEN ACCESS

Article

Upper efficiency limit of Sb_2Se_3 solar cells

Xinwei Wang,[1] Seán R. Kavanagh,[1] David O. Scanlon,[2] and Aron Walsh[1,3,4,*]

SUMMARY

Antimony selenide (Sb_2Se_3) is at the forefront of an emerging class of sustainable photovoltaic materials. Despite notable developments over the past decade, the light-to-electricity conversion efficiency of Sb_2Se_3 has reached a plateau of ~10%. Is this an intrinsic limitation of the material, or is there scope to rival the success of metal halide perovskite solar cells? Here, we assess the trap-limited conversion efficiency of Sb_2Se_3. First-principles analysis of the hole and electron capture rates for point defects in the bulk material demonstrates the critical role of vacancies as active recombination centers. We predict an upper limit of 26% efficiency in Sb_2Se_3 grown under optimal equilibrium conditions where the concentrations of charged vacancies are minimized. We further reveal how the detrimental effect of Se vacancies can be reduced by extrinsic oxygen passivation, highlighting a pathway to achieve high-performance metal selenide solar cells close to the single-junction thermodynamic limit.

INTRODUCTION

Antimony selenide (Sb_2Se_3) has attracted interest as an earth-abundant and environmental-friendly alternative among thin-film photovoltaic light absorbers, owing to its suitable electronic and optical properties.[1] Sb_2Se_3 solar cells have achieved considerable progress since they were first reported,[2,3] with a record conversion efficiency of 10.57%.[4] Nevertheless, the achieved efficiency falls far below the detailed-balance limit of ~30%[5] and lags behind the performance of other established commercial solar cells.

Similar to other emerging photovoltaic compounds, the conversion efficiency of Sb_2Se_3 is primarily limited by the large open-circuit voltage (V_{OC}) deficit.[6] Based on the detailed-balance principle,[5] the unavoidable V_{OC} deficit at 300 K due to radiative recombination is 0.2–0.3 V when the band-gap ranges from 1.0 to 1.5 eV.[7] A wide range of architectures (sensitized-[8]/planar-[9]type; substrate[10]/superstrate[4] configurations), fabrication methods (rapid thermal evaporation [RTE],[11] close space sublimation [CSS],[12] vapor transport deposition [VTD],[13] chemical bath deposition [CBD],[4] etc.), and special treatments (post-selenization[14,15] and air exposure[16,17]) have been attempted to improve the quality of Sb_2Se_3 devices. However, V_{OC} improvements have remained sluggish, with a V_{OC} deficit >0.7 V for the highest-efficiency Sb_2Se_3 solar cell.[4]

The origin of the V_{OC} bottleneck remains under debate. One potential cause is the considerable trap density in Sb_2Se_3. Defects in the absorber material reduce device performance through trap-assisted carrier recombination (Shockley-Read-Hall [SRH] recombination). Understanding the nature of the active defects is necessary to design strategies to minimize their impact. Defect characterization techniques,

CONTEXT & SCALE

When exposed to light, excess charge carriers in a solar cell should be collected at the electrical contacts to generate a photocurrent. Any failure in this collection process results in energy losses. The practical performance of solar cells is significantly influenced by trap-mediated electron-hole recombination in the bulk of the absorber layers. However, it is often unclear which defects serve as the active sites, or "killer centers," for electron-hole recombination. We showcase an approach that considers the range of defects that can form in a material and that predicts their abundance, trap levels, capture cross-sections, and ultimately the non-radiative recombination rates. Application to Sb_2Se_3 predicts that high efficiencies, comparable with the best thin-film photovoltaic absorbers, are possible.

Joule *8*, 2105–2122, July 17, 2024

such as steady-state photoluminescence (PL) emission, thermal admittance spectroscopy (TAS), deep-level transient spectroscopy (DLTS), and optical deep-level transient spectroscopy (ODLTS) can offer insights into trap levels, trap density, and defect capture cross-sections. The identification of the defect type, however, is often difficult for experiments and relies heavily on theoretical results. Point defects in Sb_2Se_3 have been widely studied by first-principles calculations,[18–23] where thermodynamic transition levels (TLs) were predicted. The community has tried to identify the most detrimental defect in Sb_2Se_3 by matching measured defect levels with theoretical results. Nevertheless, owing to the complexity of defect physics of Sb_2Se_3, there has been a debate on whether antisites or vacancies are the most detrimental "killer" imperfections.[4,10,24,25] On the other hand, defects with deep levels were proposed as potential recombination centers, but the depth alone is not a sufficient condition for rapid electron and hole capture processes.[26,27] Moreover, recent computational work has shown that global optimization of defect geometries is important to obtain the true ground-state structures and behavior (e.g., energy levels and recombination activity),[23,28] with this being particularly important in low-symmetry materials, calling into question conclusions based on singular defect relaxations.

In this work, we have investigated the intrinsic point defects in Sb_2Se_3 by using a global structure searching strategy,[23,29,30] and we have studied the non-radiative carrier capture processes by systematic first-principles calculations. The upper limit to the conversion efficiency in Sb_2Se_3 is predicted by considering both radiative and non-radiative processes in the bulk material, acting as a quantitative measure of defect tolerance. Vacancies are identified as the most detrimental recombination centers, with the largest contributions coming from V_{Se} and V_{Sb} under Se-poor and Sb-poor conditions, respectively. We conclude that Sb_2Se_3 solar cells suffer from significant non-radiative recombination, especially under extreme Sb-rich growth conditions, and higher conversion efficiencies can be achieved under intermediate growth conditions that minimize vacancy concentrations. The impact of oxygen passivation is further studied, demonstrating its effectiveness in enhancing the performance of Sb_2Se_3 by transforming the deep levels associated with detrimental Se vacancies to shallow ones. These results elucidate the loss mechanisms associated with intrinsic point defects and provide insights into optimizing the performance of Sb_2Se_3 solar cells.

RESULTS AND DISCUSSION

Equilibrium point defect population

Sb_2Se_3 adopts an orthorhombic crystal structure (space group *Pnma*/*Pbnm*, no. 62) (Figure 1). Note that *Pnma* and *Pbnm* have the same symmetry but differ in axis definitions. In this work, we use the *Pnma* setting for the Miller indexing of planes in Sb_2Se_3. The structure is composed of quasi-one-dimensional (1D) $[Sb_4\,Se_6]_n$ ribbons arranged together via weak interactions.[31] Due to the low crystal symmetry, the chemical environment for each Sb/Se element in the unit cell is different, leading to two inequivalent Sb sites and three inequivalent Se sites.

We first investigate all intrinsic point defects (i.e., vacancies, antisites, and interstitials) in Sb_2Se_3. The ShakeNBreak[29,30] structure searching workflow is applied for each defect species to identify the ground-state geometries. All inequivalent sites are considered, giving rise to five types of vacancies ($V_{Sb(1)}$, $V_{Sb(2)}$, $V_{Se(1)}$, $V_{Se(2)}$, and $V_{Se(3)}$) and five antisites ($Se_{Sb(1)}$, $Se_{Sb(2)}$, $Sb_{Se(1)}$, $Sb_{Se(2)}$, and $Sb_{Se(3)}$). Besides, nine inequivalent sites for interstitials Sb_i/Se_i (shown in Figure S1) are considered as initial

[1]Thomas Young Centre and Department of Materials, Imperial College London, Exhibition Road, London SW7 2AZ, UK

[2]School of Chemistry, University of Birmingham, Birmingham B15 2TT, UK

[3]Department of Physics, Ewha Womans University, 52 Ewhayeodae-gil, Seodaemun-gu, Seoul 03760, South Korea

[4]Lead contact

*Correspondence: a.walsh@imperial.ac.uk

https://doi.org/10.1016/j.joule.2024.05.004

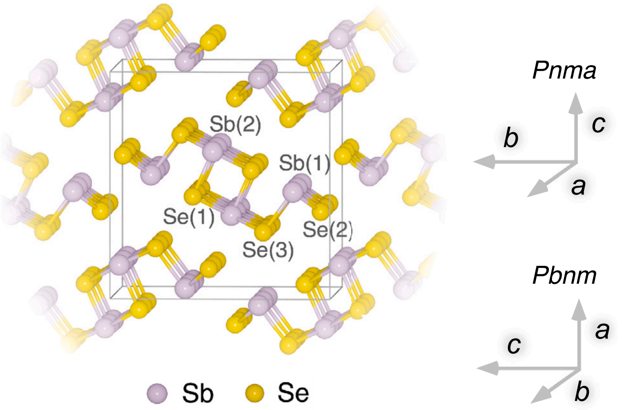

Figure 1. Ground-state crystal structure of Sb_2Se_3
The crystallographic unit cell (*Pnma*/*Pbnm* space group) is represented by a cuboid. Inequivalent sites are denoted by the atom labels enclosed in parentheses.

defect configurations by the Voronoi scheme, which is an efficient approach for sampling interstitial sites.[32,33] Subsequent geometry relaxation yields six distinct interstitial configurations for both Sb_i and Se_i. The workflow of generating and optimizing the defect structures is discussed in experimental procedures. The comparison of energies, using structure searching and local geometry optimizations, is shown in supplemental information section "comparison of global and local searches." Formation energies of all defects are calculated under different equilibrium growth conditions (Figures 2A and 2B for Sb-/Se-rich conditions and Figure S2 for Se-moderate conditions). We find that no native defects are of high energy in this system, with all being in the <2.6 eV range, which can be partly attributed to the soft crystal structure and chemical bonding—akin to lead halide perovskites.[34] One unique feature of this system is that all intrinsic point defects show amphoteric behavior, with both stable positively and negatively charged states. For defects with the lowest formation energies, all thermodynamic TLs are very deep. Moreover, defect behavior can differ significantly for different inequivalent sites. For example, $V_{Se(2)}$ exhibits an unusual four-electron negative-*U* behavior (i.e., negative electron [pair] correlation energy and two thermodynamically stable charge states differing by four electrons; $\Delta q = 4$), whereas $V_{Se(1)}$ and $V_{Se(3)}$ only show typical two-electron negative-*U* transitions ($\Delta q = 2$).[23]

The formation energies of defects change significantly as the growth conditions change from Sb-rich to Se-rich. The equilibrium defect concentration is further calculated as a function of the growth condition. As shown in Figure 2C, the dominant defects with high concentrations ($>10^{14}$ cm^{-3}) under Sb-rich (Se-rich) condition are Sb_{Se} and V_{Se} (Se_{Sb} and V_{Sb}), while the concentrations of all interstitials are low despite the open crystal structure, which agree with the previous theoretical study.[20] The antisites/vacancies benefit from energy-lowering reconstructions (valence alternation)[23] that increase their concentrations. Heavy charge compensation from the amphoteric defects results in low carrier concentrations in the dark of around 10^8 and 10^{10} cm^{-3} under Sb-rich and Se-rich conditions, respectively (Figure S3), which qualitatively match experimental observations of low carrier concentrations in Sb_2Se_3.[1]

The self-consistent Fermi level (E_F) as a function of the growth condition is shown in Figure 2D, which is pinned close to the middle of the band gap owing to strong charge compensation from the low-energy defects. With the increase of μ_{Se}, the self-consistent E_F decreases from 0.68 eV under Sb-rich conditions to 0.56 eV under

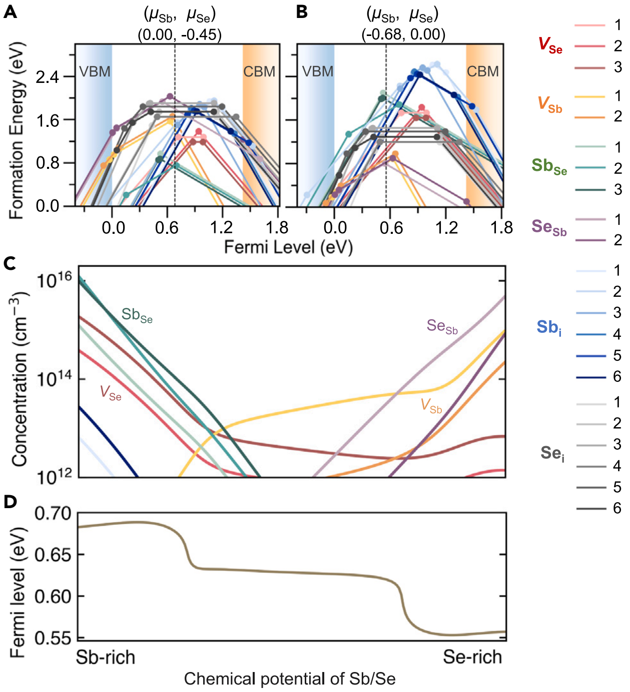

Figure 2. Calculated intrinsic point defect properties of Sb_2Se_3

(A and B) Calculated formation energies of intrinsic point defects in Sb_2Se_3 under chemical potentials that represent (A) Sb-rich and (B) Se-rich growth conditions. The charge state is denoted by the slope of the solid line, and the thermodynamic transition level corresponds to the filled circle. The valence band maximum (VBM) is set to 0 eV, and the conduction band minimum (CBM) is obtained from the calculated fundamental (indirect) band gap of 1.42 eV by the HSE06 functional. The self-consistent Fermi levels are indicated by vertical dashed lines. The numbers in the legend represent different inequivalent sites.

(C and D) (C) Equilibrium defect concentration and (D) self-consistent Fermi level (relative to the VBM) at 300 K in Sb_2Se_3 crystals grown at 550 K[4,10,22] as a function of the growth condition.

Se-rich conditions, which is in good agreement with the experimental results of 0.60 and 0.52 eV under Se-poor and Se-rich conditions, respectively.[35] Considering the calculated fundamental band gap of 1.42 eV, this indicates intrinsic weakly *p*-type conductivity, which agrees well with the naturally weak *p*-type behavior in Sb_2Se_3 reported by most studies.[9,36,37]

It is worth noting that Huang et al.[22] predicted a higher concentration of V_{Se} under Se-rich compared with Se-poor conditions by first-principles calculations, an unusual situation driven by the Fermi level changes. The main origin of this difference is our identification of low-energy positive charge states for V_{Se}, V_{Sb}, and Se_{Sb} under Se-rich conditions, using a global structure searching strategy.[23,29,30] This results in strong charge compensation and a self-consistent Fermi level near midgap (0.56 eV), which matches well with the experimental value of 0.60 eV.[35] Our predicted intrinsic midgap Fermi level corresponds to higher formation energies for V_{Se}^{2+} and thus much lower predicted V_{Se} concentrations under Se-rich conditions. We therefore find that global structure searching is necessary to accurately predict defect properties in chalcogenide semiconductors.

Non-equilibrium carrier capture

We next consider the kinetics of non-radiative carrier capture and recombination when Sb_2Se_3 is subject to above band-gap illumination. A description of the

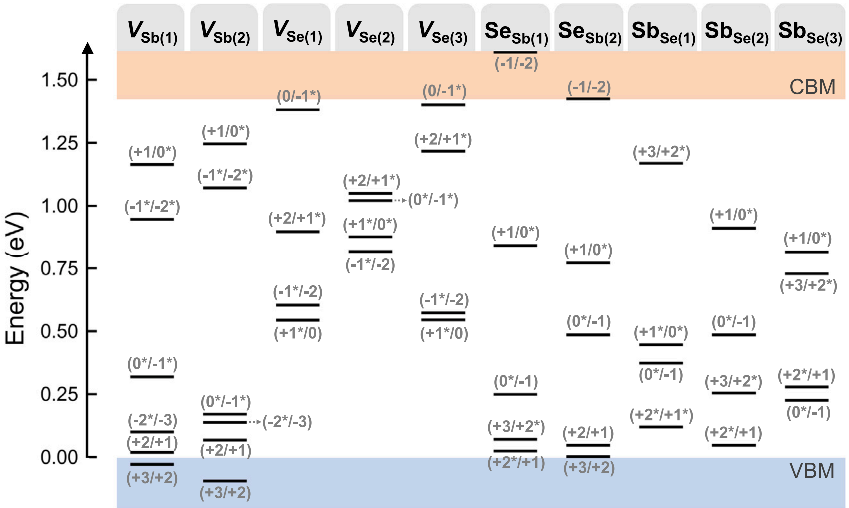

Figure 3. Charge state transition levels of point defects with high concentrations in Sb_2Se_3

Metastable charge states (which are not the thermodynamic ground state at any Fermi level; Figure 2) are indicated with asterisks (*), and the Fermi level is referenced to the valence band maximum (VBM).

microscopic processes requires going beyond the static defect properties and considering the dynamics of transitions between different charge states of a defect. This is achieved by introducing configuration coordinate (CC) diagrams that connect the initial (charge q) and final (charge q') state structures of each defect D. Trap-mediated electron-hole recombination can be considered in terms of the successive capture of electrons and holes, i.e.,

$$D^q \overset{h\nu}{\rightleftharpoons} D^q + e^- + h^+ \overset{-\hbar\omega}{\rightleftharpoons} D^{q'} + h^+ \overset{-\hbar\omega}{\rightleftharpoons} D^q \qquad \text{(Equation 1)}$$

where the excess electronic energy provided by light absorption ($h\nu$) is thermally emitted through phonons ($\hbar\omega$).

We start by considering the single-electron transitions for those defects with high concentrations (i.e., all vacancies and antisites). The single-electron transition energy levels are shown in Figure 3. Multiple inequivalent sites and accessible charge states make the defect levels in Sb_2Se_3 complex to analyze. Different TLs share similar energy ranges as shown in Figure 3. Consequently, it is difficult to identify the defect species solely based on the comparison of energy levels with values that are measured experimentally. Since our objective is to identify potential recombination centers with both rapid electron and hole capture, shallow defect levels (i.e., where the defect level and band-edge energy difference is comparable to the thermal energy $k_B T$) are excluded from consideration.

The complete pathways for trap-mediated electron and hole capture by point defects, including those introduced by low-energy metastable states (shown to be important for accurate predictions[38]), are mapped (shown in Figure S4). The dominant charge capture transition under most growth conditions, having both high defect concentrations and large electron and hole capture coefficients, is predicted to be $V_{Se(2)}^{2+} \leftrightarrow V_{Se(2)}^{+}$. The corresponding atomic structures and potential energy surfaces (PESs) are shown in Figure 4. Structures and PESs for other charge capture transitions can be found in section "carrier capture processes" of supplemental

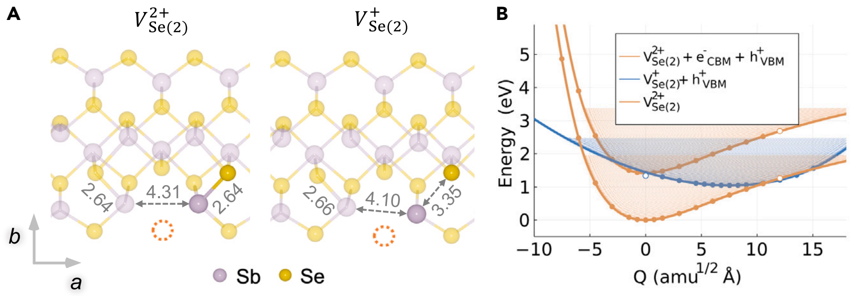

Figure 4. Carrier capture process of $V_{Se(2)}^{2+}$ and $V_{Se(2)}^{+}$

(A) Defect configurations of $V_{Se(2)}^{2+}$ and $V_{Se(2)}^{+}$. The bond lengths in Å are labeled, and the vacant Se site is denoted by a dotted circle.

(B) One-dimensional configuration coordinate diagram for charge transitions between $V_{Se(2)}^{2+}$ and $V_{Se(2)}^{+}$. Solid circles are data points obtained by DFT calculations and used for fitting, while hollow circles are discarded for fitting due to charge delocalization (see section "$V_{Se}^{2+} \leftrightarrow V_{Se}^{+}$" of supplemental information). Solid lines represent best fits to the data.

information. Table 1 shows the carrier capture coefficients and cross-sections at room temperature and key parameters used in the calculations.

The mass-weighted displacement ΔQ represents the structural difference between the two defect charge states involved in the charge capture process. The main contribution to ΔQ of 7.52 amu$^{1/2}$Å for $V_{Se(2)}^{2+}$ and $V_{Se(2)}^{+}$ comes from the shortening/lengthening of one Sb–Se bond length beside $V_{Se(2)}$ (highlighted in Figure 4A) during the hole/electron capture process. PESs were mapped by performing single-point density functional theory (DFT) calculations for interpolated configurations between the equilibrium structures of $V_{Se(2)}^{2+}$ and $V_{Se(2)}^{+}$ (Figure 4A). The electronic eigenstates at each Q were checked (Figure S6) to remove any data points where the occupation of single-particle defect levels changed due to crossing the band edges (i.e., charge delocalization) from fitting. The equilibrium structure of $V_{Se(2)}^{2+}$ is set as a reference with $Q = 0$ amu$^{1/2}$Å and E = 0 eV. The equilibrium structure of $V_{Se(2)}^{+}$ is offset horizontally by ΔQ and vertically by $\Delta E = 1.05$ eV (which corresponds to position of the (+2/+1) TL with respect to the valence band maximum [VBM]). The uppermost orange curve ($V_{Se(2)}^{2+} + e^- + h^+$) is vertically upshifted by the fundamental band gap E_g, compared with the bottom-most orange curve ($V_{Se(2)}^{2+}$), corresponding to the energy of the photo-excited electron-hole pair. Further details regarding the calculation of carrier capture coefficients via the CC approach are given in experimental procedures.

In the process of non-radiative capture of an electron by $V_{Se(2)}^{2+}$, the initial (excited) state is represented by the uppermost orange curve, and the final (ground) state corresponds to the blue curve. The two PESs intersect at $\Delta E_b = 2$ meV above the minimum of the excited state. The negligible ΔE_b and large phonon overlap result in a large electron capture coefficient (C_e) of 5.63×10^{-6} cm^3 s^{-1} at room temperature. In the non-radiative capture of a hole by $V_{Se(2)}^{+}$, the initial and final states correspond to the blue and bottom-most orange curves, respectively. A weaker Coulomb repulsion of positively charged holes by $V_{Se(2)}^{+}$ (included in the scaling factor $s(T)f$), reduced pathway degeneracy g, and larger ΔE_b of 83 meV (Table 1) all contribute to a smaller hole capture coefficient (C_h) of 1.22×10^{-8} cm^3 s^{-1} at room temperature. Therefore, electron-hole carrier recombination at $V_{Se(2)}$ is limited by the hole

Table 1. Key parameters used to calculate the carrier capture coefficients in the transition of $V_{\mathrm{Se(2)}}^{2+} \leftrightarrow V_{\mathrm{Se(2)}}^{+}$

ΔQ	Capture process	ΔE_b	g	W_{if}	$s(T)f$	C	σ
7.52	electron	2	4	1.81×10^{-2}	2.09	5.63×10^{-6}	2.85×10^{-13}
	hole	83	1	1.76×10^{-2}	0.35	1.22×10^{-8}	9.89×10^{-16}

Mass-weighted distortion ΔQ (amu$^{1/2}$Å), energy barrier ΔE_b (meV), degeneracy factor g of the final state, electron-phonon coupling matrix element W_{if}, and scaling factor $s(T)f$ at 300 K, along with calculated capture coefficient C (cm^3 s^{-1}) and cross-section σ (cm^2) at 300 K.

capture process $V_{\mathrm{Se(2)}}^{+} + \mathrm{h}^{+} \rightarrow V_{\mathrm{Se(2)}}^{2+}$. The calculated capture cross-sections (σ) agree well with the range of experimental results (10^{-17}–10^{-13} cm^2).[4,13]

Trap-limited conversion efficiency

To directly quantify the impact of electron-hole recombination at point defects on the Sb_2Se_3 solar cell performance, the upper limit to efficiency is predicted using the trap limited conversion (TLC) model.[39,40] Detailed equations can be found in experimental procedures. Current density-voltage ($J - V$) curves of Sb_2Se_3 solar cells are predicted under different growth conditions including both radiative and non-radiative recombination (Figure 5A). Directionally averaged optical absorption coefficients are used when calculating the radiative limit, considering the polycrystalline nature of most Sb_2Se_3 samples from the literature. The film thickness is set to 500 nm, which has been found to maximize short-circuit current density (J_{SC}) experimentally.[41] As shown in Figure 5A, J_{SC} is predicted to be 26.4 mA/cm^2, which is lower than the J_{SC} of 33.5 mA/cm^2 achieved in the highest-efficiency Sb_2Se_3 solar cell.[4] This difference is due to the neglect of temperature effects, which would further increase the calculated J_{SC}. V_{OC} deficit (defined as $E_g/q - V_{OC}$) due to radiative recombination is predicted to be 0.14 V. Non-radiative recombination is found to significantly contribute to V_{OC} deficit, with predicted total deficits of 0.54 V and 0.35 V under Sb-rich and Se-rich conditions, respectively (Figure 5A).

The vital role of growth conditions in device performance has been widely reported by experiments, with selenization treatment being proven effective in improving the conversion efficiency of Sb_2Se_3 by reducing the concentration of V_{Se}.[14,42] Thus, we study the V_{OC} loss due to non-radiative recombination ($\Delta V_{OC}^{\mathrm{non-rad}}$) as a function of the growth condition (Figure 5B). The largest $\Delta V_{OC}^{\mathrm{non-rad}}$ of 0.41 V is obtained under Sb-rich/Se-poor conditions. With the increase of the Se chemical potential μ_{Se} (corresponding to more Se-rich conditions), $\Delta V_{OC}^{\mathrm{non-rad}}$ initially decreases until reaching a minimum (with the lowest $\Delta V_{OC}^{\mathrm{non-rad}}$ of 0.09 V achieved under intermediate growth conditions), and then it increases again until reaching the Se-rich limit. Nevertheless, $\Delta V_{OC}^{\mathrm{non-rad}}$ is much smaller under Se-rich conditions (0.21 V) than under Sb-rich conditions (0.41 V). This trend agrees well with experimental findings,[14,15,42] including the efficiency decrease that occurs under extremely Sb-/Se-rich conditions.[43]

To further analyze the most detrimental defect species, we divide the contributions to $\Delta V_{OC}^{\mathrm{non-rad}}$ based on each defect. Considering that the total $\Delta V_{OC}^{\mathrm{non-rad}}$ is not exactly a simple sum of individual defect contributions (as these depend on the total recombination rate), we normalize the colored areas in Figure 5B by:

$$\Delta V_{\mathrm{OC\_contribution}}^{\mathrm{non-rad}} = \frac{\Delta V_{\mathrm{OC\_individual}}^{\mathrm{non-rad}}}{\sum \Delta V_{\mathrm{OC\_individual}}^{\mathrm{non-rad}}} \times \Delta V_{\mathrm{OC\_total}}^{\mathrm{non-rad}} \qquad \text{(Equation 2)}$$

As shown in Figure 5B, we find that the conversion efficiency of Sb_2Se_3 is limited by vacancies, whereas antisites have a negligible impact on non-radiative

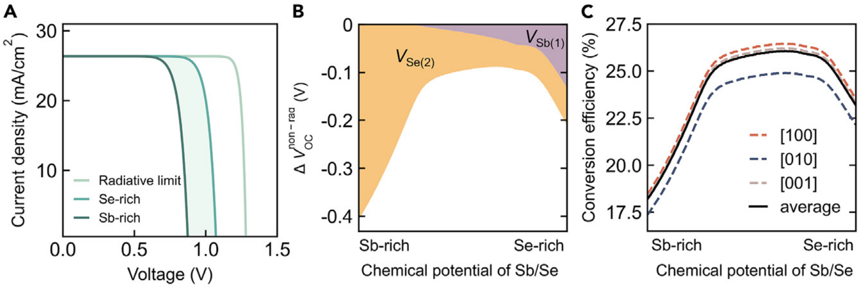

Figure 5. Prediction of first-principles trap-limited conversion efficiency

(A) Calculated current density-voltage ($J - V$) curves for Sb_2Se_3, assuming the radiative limit (only band-to-band radiative recombination losses) and including defect-induced non-radiative recombination under Se-/Sb-rich growth conditions. The radiative limit is calculated by averaging the optical absorption coefficients along [100], [010], and [001] crystallographic directions.

(B) V_{OC} deficit contributed by non-radiative recombination ($\Delta V_{OC}^{non-rad}$) in undoped Sb_2Se_3 as a function of growth condition, decomposed into individual defect contributions. $\Delta V_{OC}^{non-rad}$ is defined as the difference between the values of V_{OC} and V_{OC}^{rad}. Defect species with $\Delta V_{OC}^{non-rad} < 0.05$ V are not shown.

(C) Trap-limited conversion efficiency as a function of the growth condition. [100], [010], and [001] correspond to the crystallographic directions in Sb_2Se_3. All results shown correspond to a film thickness of 500 nm and room-temperature defect concentrations assuming an annealing temperature of 550 K.[4,10,22]

recombination. This calls into question the prevailing assumption of antisites being the most detrimental defects to Sb_2Se_3 solar cell performance.[4,10,19] Indeed, the concentrations of antisites are highest among all defect species (Figure 2C), and they do introduce deep defect levels in the band gap (Figure 3). Nevertheless, our calculated low to moderate non-radiative carrier capture coefficients (Figure S4) suggest that antisites are benign with low recombination rates.

Among all vacancies, $V_{Se(2)}$ and $V_{Sb(1)}$ contribute most to $\Delta V_{OC}^{non-rad}$ under Sb-rich and Se-rich conditions, respectively (Figure 5B), indicating that these defect species should be avoided to improve the photo-conversion efficiency in Sb_2Se_3. $V_{Se(2)}$ in particular is the most detrimental defect species because of its high defect concentration and large carrier capture coefficients for both electron and hole capture (Figure 2C; Table 1), while $V_{Se(1)}$ and $V_{Se(3)}$ are found to have negligible impacts on efficiency. This highlights the sensitivity of carrier trapping and recombination to small changes in structures/energetics and, consequently, the significant variation in behavior that different inequivalent sites of the same nominal defect (e.g., Se vacancies; V_{Se}) can exhibit. The PESs and calculated capture coefficients for the other two inequivalent sites of V_{Se} are shown in Figure S5 and Table S2, respectively.

Using the TLC model,[39,40] the upper limit to conversion efficiency in Sb_2Se_3 solar cell is predicted as shown in Figure 5C. Considering that the control of film orientation has been widely reported to improve the conversion efficiency of Sb_2Se_3 solar cells,[11,44,45] the directionally dependent (anisotropic) conversion efficiency is also calculated based on the respective optical absorption coefficients (Figure S18). The orientation dependence of efficiency is calculated by considering unpolarized sunlight incident along each of the three crystallographic axes in Sb_2Se_3. We predict that the highest trap-limited conversion efficiency of 26.5% can be achieved along the [100] direction (which is the direction along the quasi-1D $[Sb_4\ Se_6]_n$ ribbons) under the optimal Se-moderate growth conditions. Experiments have also found Sb_2Se_3 films with controlled orientation along this direction to maximize device

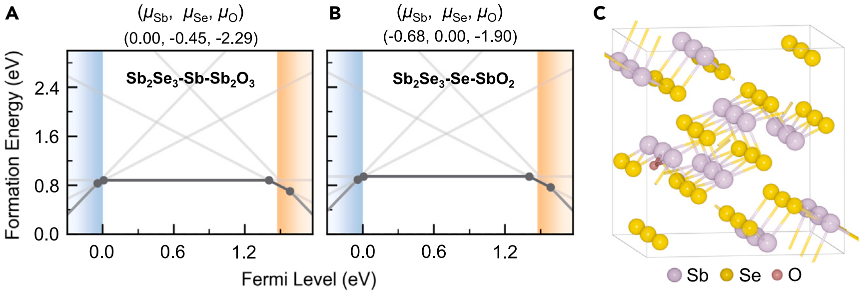

Figure 6. Calculated defect properties of oxygen substitution in Sb_2Se_3

(A and B) Formation energies of $O_{Se(2)}$ in Sb_2Se_3 under (A) Sb-rich (with Sb_2O_3 being the oxygen-limiting phase) and (B) Se-rich (with SbO_2 being the oxygen-limiting phase) conditions. The dark gray lines indicate energetically most favorable charge states.

(C) Defect configuration of $O^0_{Se(2)}$.

efficiencies.[11,46] Under the same conditions, the maximum difference in efficiency along different directions is 1.6%. These results are calculated based on equilibrium defect concentrations at an annealing temperature of 550 K, matching previous theoretical studies[22] and representing an average value of the range used in the synthesis of champion Sb_2Se_3 devices.[4,10] A high annealing temperature of 648 K is reported to benefit the crystalline quality in the highest-efficiency Sb_2Se_3 solar cell.[4] However, a higher annealing temperature will increase defect concentrations (assuming equilibrium under annealing) and thus further reduce the trap-limited conversion efficiency (Figure S19).

Extrinsic passivation of deep defects

To investigate potential strategies for reducing the impact of Se vacancies in Sb_2Se_3, we further study the effect of oxygen substitution. The focus on O_{Se} is inspired by the experimental observation that oxygen exposure is beneficial to Sb_2Se_3 solar cell performance,[16,17] as well as our calculated result that the conversion efficiency of Sb_2Se_3 is largely limited by V_{Se}. As shown in Figure 5B, V_{Se} is the only intrinsic point defect species found to significantly lower the efficiency under Sb-rich conditions and also to play an important role even under Se-rich conditions, owing to its relatively high concentration ($>10^{12}$ cm^{-3}). Thus, it is intuitive to surmise that detrimental Se vacancies could be passivated by O_2 upon oxygen exposure.

To test our hypothesis and understand the role of oxygen, the structural configuration and energy of O_{Se} formation are studied. We mainly focus on the second inequivalent site of Se as $V_{Se(2)}$ is responsible for >99% of the contribution to ΔV_{OC} among all Se vacancies. As shown in Figure 6, the neutral state of $O_{Se(2)}$ is thermodynamically stable across almost the entire band gap, leading to shallow defect levels—which are inactive for recombination. Moreover, the formation energies of $O^0_{Se(2)}$ under O-poor conditions are relatively low (~0.8 eV, which is similar to the formation energy of $V_{Se(2)}$). These results suggest the role of oxygen in passivating Se vacancies and eliminating their detrimental effects by shifting the deep recombination-active levels of $V_{Se(2)}$ (Figure 3) to shallow inactive ones.

Current limitations and future extensions

While our approach improves upon the efficiency limits estimated by established metrics such as the detailed-balance limit[5] and spectroscopic limited maximum efficiency (SLME),[47] we note that there are several limitations:

(1) The underlying electronic structure calculations are athermal, and effects such as lattice thermal expansion and electron-phonon interactions are currently neglected. One consequence is that the calculated fundamental band gap of 1.4 eV is larger than the typical room-temperature experimental values for Sb_2Se_3 in the 1.0–1.3 eV range.[48,49]

(2) The carrier mobility is not considered and inherently assumed to be infinite. The effect of mobility on efficiency is negligible for photovoltaic (PV) absorbers with high mobility and thin layers.[50]

(3) The impacts of extrinsic defects and surface/interface electron-hole recombination, which are determined by specific materials processing and device architectures, have not been considered. We note that these factors could also contribute to V_{OC} loss in practical devices.

Conclusions

While structurally complex crystals such as Sb_2Se_3 can support the formation of many types of charged point defects, we have shown that only a subset will have a significant equilibrium population. Vacancies and antisites are shown to be the dominant point defects in Sb_2Se_3 with high concentrations ($>10^{12}$ cm^{-3}), while the concentrations of interstitials are relatively low. Furthermore, by considering the processes of electron and hole capture, the most detrimental defects can be identified based on first-principles calculations. This approach yields the ability to predict an upper limit for light-to-electricity conversion efficiency in a solar cell, based on the bulk properties of the absorber material. For Sb_2Se_3, V_{Se} and V_{Sb} contribute most to V_{OC} deficit under Sb-rich and Se-rich conditions, respectively. The largest V_{OC} deficit is predicted to be 0.54 V under Sb-rich conditions with a conversion efficiency of 18%. Intermediate growth conditions result in lower concentrations of defects and thus higher conversion efficiency (26%). Therefore, to improve the device performance, it is critical to suppress vacancy formation and optimize the growth conditions. As a proof of concept, we showed that the detrimental effects of Se vacancies can be reduced by oxygen passivation (i.e., the formation of O_{Se}). An alternative passivation strategy is Fermi-level engineering, where an extrinsic donor dopant is introduced during crystal growth/annealing to push the Fermi level higher in the gap, increasing the formation energy of V_{Se}^{2+} and thus reducing its concentration. Considering the similar quasi-1D structures and optoelectronic structures, the insights gained from Sb_2Se_3 could be transferable to the $Sb_2(S,Se)_3$ system, where similar defect processes are expected to be at play. In conclusion, our work provides a microscopic understanding of the efficiency limit of Sb_2Se_3 solar cells.

EXPERIMENTAL PROCEDURES

Resource availability

Lead contact

Further information and requests for resources should be directed to and will be fulfilled by the lead contact, Prof. Aron Walsh (a.walsh@imperial.ac.uk).

Materials availability

This study did not generate new unique materials.

Data and code availability

The defect configurations with the lowest energies for each charge state, as well as corresponding input and output files, have been uploaded to the NOMAD Repository and are freely available at https://doi.org/10.17172/NOMAD/2024.04.25-1. All open-source codes used in the study, including doped, CarrierCapture.jl, and ShakeNBreak, are referenced in the paper and available on GitHub.

Computational methods

Trap-limited conversion efficiency

The light-to-electricity conversion efficiency of a solar cell depends on the proportion of electron-hole pairs extracted from the absorber layer and is limited by different electron-hole recombination mechanisms. In this work, trap-limited conversion efficiency of a single-junction solar cell is determined by considering radiative and non-radiative recombination processes, following the methodology proposed by Kim et al.[39] and Kim and Walsh.[40] The effects of band gap, (film) thickness-dependent optical absorption, and defect properties are taken into account. The mobility of electron-hole pairs is assumed to be infinitely high, so scattering mechanisms are neglected. This assumption can be justified by the relatively high carrier mobility reported in Sb_2Se_3.[51] Recombination at surfaces and interfaces is beyond the scope of this work and thus not considered in the following.

Radiative recombination. An excited electron in the conduction band (CB) can recombine with a hole in the valence band (VB) and energy is released as photons. This is an unavoidable process known as radiative recombination, which is an inverse process of light absorption.

Under the assumption of ideal reflection at the bottom of the absorber, the photon absorptivity a is calculated by[52]

$$a(E;W) = 1 - e^{-2\alpha(E)W} \qquad \text{(Equation 3)}$$

where E and W are the photon energy and film thickness, respectively, and α is the optical absorption coefficient.

Assuming that each absorbed photon generates one electron-hole pair, the short-circuit current J_{SC} is given by[39]

$$J_{SC}(W) = e\int_{E_g}^{\infty} a(E;W)\Phi_{sun}(E)\mathrm{d}E \qquad \text{(Equation 4)}$$

where e is the elementary charge; $\Phi_{sun}(E)$ is incident spectral photon flux density at the photon energy E. Here, a standard AM1.5 solar spectrum is considered.

The radiative recombination rate R_{rad} at temperature T and voltage V is given by[39]

$$\begin{aligned} R_{rad}(V) &= \frac{2\pi}{c^2h^3}\int_0^{\infty} a(E;W)\left[e^{\frac{E-eV}{k_BT}} - 1\right]^{-1} E^2\mathrm{d}E \\ &\approx \frac{2\pi}{c^2h^3}e^{\frac{eV}{k_BT}}\int_0^{\infty} a(E;W)\left[e^{\frac{E}{k_BT}} - 1\right]^{-1} E^2\mathrm{d}E \end{aligned} \qquad \text{(Equation 5)}$$

The net current density J^{rad} generated under illumination in the radiative limit is given by[39]

$$J^{rad}(V;W) = J_{SC}(W) + J_0^{rad}(W)\left(1 - e^{\frac{eV}{k_BT}}\right) \qquad \text{(Equation 6)}$$

where the saturation current is $J_0^{rad} = e\,R_{rad}(0)$.

Non-radiative recombination. The main cause of efficiency loss in a solar cell usually involves non-radiative recombination facilitated by deep-level defects. Identifying the detrimental defect species is thus crucial to improving photovoltaic device performance.

Defect formation energy. The formation energy of a point defect D in charge state q is calculated by the equation[53,54]

$$\Delta E^f_{D,q} = E_{D,q} - E_{\text{host}} - \sum_i n_i\mu_i + qE_F + E_{\text{corr}} \quad \text{(Equation 7)}$$

where $E_{D,q}$ and E_{host} are the total energies of the supercells with and without the defect D, respectively. n_i and μ_i represent the number and the chemical potential of added ($n_i > 0$) or removed ($n_i < 0$) atom of type i, respectively. E_F is the Fermi level. E_{corr} accounts for the finite-size corrections for charged defects under periodic boundary conditions. In this work, the correction scheme developed by Kumagai and Oba,[55] which accounts for anisotropic dielectric screening, is employed and has been extensively shown to be both accurate and robust.[56,57]

Defect TL. The thermodynamic charge TL $\varepsilon(q_1/q_2)$ is defined as the Fermi-level position at which the formation energies of charge states q_1 and q_2 of a defect are the same, and it can be obtained from the relation

$$\varepsilon(q_1 / q_2) = \frac{\Delta E^f_{D,q_1}(E_F = 0) - \Delta E^f_{D,q_2}(E_F = 0)}{q_2 - q_1} \quad \text{(Equation 8)}$$

where $\Delta E^f_{D,q}(E_F = 0)$ is the formation energy of a defect D in the charge state q when the Fermi level is at the VBM.

Defect and charge carrier concentration. The self-consistent Fermi level is calculated by an iterative method[58,59] based on the charge neutrality condition

$$\sum_{D,q} qC_{D,q} - n_0 + p_0 = 0 \quad \text{(Equation 9)}$$

where $C_{D,q}$ is the defect concentration of a defect D in its accessible charge state q. n_0 and p_0 are concentrations of free electrons and holes, respectively.

The defect concentration $C_{D,q}$ is given as

$$C_{D,q} = gN_D e^{\frac{-\Delta E^f_{D,q}}{k_B T_{\text{anneal}}}} \quad \text{(Equation 10)}$$

where g is the degeneracy term including spin and geometry degeneracy. N_D is the number of possible sites for defect D to form in the supercell per volume. k_B is the Boltzmann constant, and T_{anneal} is the temperature at which the host material is annealed/synthesized.

The electron (n_0) and hole (p_0) concentrations are obtained by

$$n_0 = \int_{E_{\text{CBM}}}^{\infty} \rho(E)f(E)dE \quad \text{(Equation 11)}$$

$$p_0 = \int_{-\infty}^{E_{\text{VBM}}} \rho(E)[1 - f(E)]dE \quad \text{(Equation 12)}$$

where $\rho(E)$ is the density of states (DOS) per unit volume, and $f(E)$ is the Fermi-Dirac distribution function that represents the likelihood of an electron occupying an energy state E

$$f(E) = \frac{1}{e^{1+\frac{E-E_F}{k_B T}}} \quad \text{(Equation 13)}$$

where E_F is the Fermi level, and T is the temperature.

It is worth noting that T_{anneal} and T are specified as different values in this work. After rapid quenching, defects usually become "frozen in" at annealing temperature by kinetic barriers. Therefore, the defect concentrations are fixed at T_{anneal}, while the change of charge states of the same defect species is possible, and the concentrations of free electrons and holes re-equilibrate until the charge neutrality condition is met at the measurement temperature T.

Carrier capture coefficient. The non-radiative carrier capture for deep-level defects can be simulated via multiphonon emission (MPE) from first-principles calculations.[60] Within the framework of MPE, the transition between a delocalized bulk state and localized defect state can be treated by considering electron-phonon coupling as a first-order perturbation. The carrier capture coefficient is determined using Fermi's golden rule

$$C = \frac{2\pi}{\hbar} Vg \sum_{m} \omega_m \sum_{n} \left| \Delta H^{e-ph}_{im;fn} \right|^2 \delta(E_{im} - E_{fn}) \qquad \text{(Equation 14)}$$

where V is the volume of the supercell. g is the degeneracy term accounting for the number of equivalent transition pathways, which includes spin and geometry degeneracy.[38] n and m are quantum numbers of ionic states. ω_m represents the thermal occupation. $E_{\{im,fn\}}$ are total energies. $\Delta H^{e-ph}_{im;fn}$ is the electron-phonon coupling matrix element. Under the linear-coupling approximation, the matrix element is determined by Taylor expansion in Q around Q_0 with only the first-order terms preserved

$$\Delta H^{e-ph}_{im;fn} = \sum_{k} \langle \Psi_i | \partial \widehat{H} / \partial Q_k | \Psi_f \rangle \langle \chi_{im} | Q_k - Q_{0;k} | \chi_{fn} \rangle \qquad \text{(Equation 15)}$$

where $\Psi_{\{i,f\}}$ are the many-body electronic wave functions, and $\chi_{\{im,fn\}}$ are the ionic wave functions. It sums all phonon modes Q_k.

Under the effective-1D approximation, one effective phonon mode that represents the strongest interaction with the deformation of defect configuration is used. Using Kohn-Sham DFT, many-body Hamiltonian and wave functions are replaced by single-particle ones. Thus, the carrier capture coefficient is calculated by

$$\tilde{C} = \frac{2\pi}{\hbar} Vg \sum_{m} \omega_m \langle \psi_i | \partial \widehat{h} / \partial Q | \psi_f \rangle \sum_{n} \left| \langle \chi_{im} \middle| Q - Q_0 | \chi_{fn} \rangle \right|^2 \delta(\Delta E + m\hbar\Omega_i - n\hbar\Omega_f)$$

(Equation 16)

where $\hbar$ and $\psi_{\{i,f\}}$ are the single-particle Hamiltonian and single-particle wave functions, respectively. $\Omega_{\{i,f\}}$ are the phonon frequencies of initial and final states. A 1D generalized coordinate Q is used to represent atomic deformation,[61] which is defined as

$$Q^2 = \sum_{\alpha} M_\alpha \Delta R_\alpha^2 \qquad \text{(Equation 17)}$$

where M_α and ΔR_α are the mass and the displacement between the initial and final states of an atom α, respectively.

Two types of scaling parameters are considered in this work to correct the capture coefficients when necessary and were calculated using Nonrad.[62] In the cases of carrier captured by a charged defect, the Sommerfeld parameter $s(T)$[63] is calculated to account for the Coulombic interaction between the delocalized carrier and charged defect. When a charged defect supercell is used to calculate the electron-phonon matrix elements, a scaling factor f is calculated to correct the charge density near the defect. After taking into account the scaling parameters, the carrier capture coefficient is given as

$$C = s(T)f\tilde{C} \tag{Equation 18}$$

The capture cross-section σ is given by

$$\sigma = \frac{C}{\langle v \rangle} \tag{Equation 19}$$

where $\langle v \rangle = \sqrt{3k_BT/m^*}$ is the average thermal velocity of the carrier. m^* is the average effective mass, and in this work, $m_e^* = 0.35$ and $m_h^* = 0.90$.[31]

Non-radiative recombination rate. For non-degenerate semiconductors, non-radiative recombination rate R_{SRH} under steady-state conditions is calculated based on SRH statistics[64,65]

$$R_{\mathrm{SRH}} = \frac{np - n_0p_0}{(n+n_1)\tau_p+(p+p_1)\tau_n} \tag{Equation 20}$$

where n and p are concentrations of electrons and holes, respectively. n_0 and p_0 are concentrations of electrons and holes at thermal equilibrium, respectively. $n_1 = N_c \exp\left(\frac{E_t - E_{\mathrm{CBM}}}{k_BT}\right)$ and $p_1 = N_v\exp\left(\frac{E_{\mathrm{VBM}} - E_t}{k_BT}\right)$ are electron and hole densities when the Fermi level lies at the trap level E_t, and N_c and N_v are effective DOSs for CB and VB, respectively. τ_p and τ_n are lifetime for hole and electron capture, respectively, which are given by

$$\begin{aligned} \tau_p &= \frac{1}{N_TC_p} \\ \tau_n &= \frac{1}{N_TC_n} \end{aligned} \tag{Equation 21}$$

where C_p and C_n are hole and electron capture coefficients, respectively. N_T is the total defect concentration. The relative defect concentration for a defect D in a certain charge state q is calculated under kinetic equilibrium. For example, in the transitions between q, $q-1$ and $q-2$ charge states:

$$D^q \underset{h^+}{\overset{e^-}{\rightleftharpoons}} D^{q-1} \underset{h^+}{\overset{e^-}{\rightleftharpoons}} D^{q-2} \tag{Equation 22}$$

Under steady-state conditions (constant illumination), the net electron capture rate by $D^q(D^{q-1})$ should be equal to the net hole capture rate by $D^{q-1}(D^{q-2})$. In Sb_2Se_3, the equilibrium carrier density n_0 or p_0 is much lower than the photo-generated carrier density Δn, and carrier emission is assumed to be negligible for deep-level defects[66]:

$$\begin{aligned} N^qC_n^q\Delta n &= N^{q-1}C_p^{q-1}\Delta n \\ N^{q-1}C_n^{q-1}\Delta n &= N^{q-2}C_p^{q-2}\Delta n \end{aligned} \tag{Equation 23}$$

The sum of concentrations of D^q, D^{q-1}, and D^{q-2} is kept fixed and determined by the concentration of D at thermodynamic equilibrium (N_{tot}). The relative defect concentrations are then calculated as

$$\begin{aligned} N^{q-1} &= \frac{N_{\mathrm{tot}}}{1+\frac{C_p^{q-1}}{C_n^q}+\frac{C_n^{q-1}}{C_p^{q-2}}} \\ N^q &= N^{q-1}\frac{C_p^{q-1}}{C_n^q} \\ N^{q-2} &= N^{q-1}\frac{C_n^{q-1}}{C_p^{q-2}} \end{aligned} \tag{Equation 24}$$

The total SRH recombination rate R_{SRH} is the sum of recombination rates for all defect charge states.

Upon illumination, there is an extra contribution of photo-generated carrier concentration Δn, which is given by

$$\Delta n = \frac{1}{2}\left[-n_0 - p_0 + \sqrt{(n_0+p_0)^2 - 4n_0p_0\left(1 - e^{\frac{eV}{k_BT}}\right)}\right] \qquad \text{(Equation 25)}$$

Consequently, the concentrations of electrons n and holes p are calculated by

$$\begin{aligned} n &= n_0 + \Delta n \\ p &= p_0 + \Delta n \end{aligned} \qquad \text{(Equation 26)}$$

Trap-limited conversion efficiency. By including both radiative and non-radiative recombination, the net current density J under a bias voltage V is defined as

$$J(V;W) = J_{\mathrm{SC}}(W) + J_0^{\mathrm{rad}}(W)\left(1 - e^{\frac{eV}{k_BT}}\right) - eR_{\mathrm{SRH}}(V)W \qquad \text{(Equation 27)}$$

The maximum efficiency is defined as the ratio of the maximum power density to the incident light power density, which is given by

$$\eta_{\max} = \max_V\left(\frac{JV}{e\int_0^{\infty} E\Phi_{\mathrm{sun}}(E)\mathrm{d}E}\right) \qquad \text{(Equation 28)}$$

First-principles calculations

All calculations for the underlying total energies were performed based on Kohn-Sham DFT[67,68] as implemented in Vienna Ab initio Simulation Package (VASP).[69] The projector augmented-wave (PAW) method[70] was employed with converged plane-wave energy cutoffs of 350 and 400 eV for Sb_2Se_3 with intrinsic defects and extrinsic oxygen defects, respectively, which are consistent with previous studies.[19,71,72] Both structural relaxation and static calculations of the pristine structure and defects in Sb_2Se_3 were performed using the Heyd-Scuseria-Ernzerhof hybrid exchange-correlation functional (HSE06)[73,74] and the D3 dispersion correction,[75] which have been demonstrated to reproduce the geometric and electronic properties in Sb_2Se_3 well.[31] Spin-orbit coupling effects were not included owing to the negligible impact on Sb_2Se_3.[76]

Bulk crystal modeling. The bulk structure calculation of Sb_2Se_3 was carried out using a unit cell containing 20 atoms with $15 \times 6 \times 6$ Γ-centered Monkhorst-Pack k-point mesh. The atomic positions were optimized until the Hellman-Feynman forces on each atom were below 5×10^{-4} eV/Å.

Defect modeling. The doped Python package (v0.0.7)[77] was used for the generation, parsing, and analysis/plotting of defect supercell calculations. Defects were simulated using a ($11.86 \times 11.55 \times 11.93$ Å) 60-atom supercell, which proved to be sufficient for this system[18,19,21,72,78] considering the relatively small charge corrections due to large dielectric constants in Sb_2Se_3.[31] The convergence criterion of forces on each atom was set to 0.01 eV/Å. For both geometry optimization and static calculations, spin polarization was turned on and a $2\times2\times2$ Γ-centered k-point mesh was used. The ShakeNBreak[29] global structure searching method was used to aid the identification of ground-state defect geometries. Initial defect configurations were obtained by local bond distortions (of both compression and stretching between 0% and 60% with 10% as an interval) around the defect and random displacement (d) to all atoms in the supercell, which proved to efficiently map complex defect

PESs and to identify ground-state structures.[30] d is stochastically selected from a normal distribution of a standard deviation σ,

$$d \leftarrow \frac{1}{\sigma\sqrt{2\pi}}\exp\left(-\frac{d^2}{2\sigma^2}\right) \quad \text{(Equation 29)}$$

σ = 0.25, 0.20, and 0.15 Å were tested.

The defect and charge carrier concentrations under thermodynamic equilibrium are calculated using py-sc-fermi.[58,59] Anharmonic carrier capture coefficients were calculated using CarrierCapture.jl.[79]

SUPPLEMENTAL INFORMATION

Supplemental information can be found online at https://doi.org/10.1016/j.joule.2024.05.004.

ACKNOWLEDGMENTS

X.W. thanks Sunghyun Kim, Menglin Huang, and Shiyou Chen for valuable discussions on carrier capture processes. Via our membership of the United Kingdom's HEC Materials Chemistry Consortium, which is funded by EPSRC (EP/X035859/1), this work used the ARCHER2 UK National Supercomputing Service (http://www.archer2.ac.uk). This work was supported by EPSRC project EP/X037754/1. X.W. acknowledges Imperial College London for support via a President's PhD Scholarship. S.R.K. acknowledges funding from Samsung Electronics Ltd. (SAIT).

AUTHOR CONTRIBUTIONS

Conceptualization, X.W. and A.W.; investigation, X.W.; formal analysis, X.W.; methodology, X.W., S.R.K., D.O.S., and A.W.; visualization, X.W.; writing – original draft, X.W.; writing – review & editing, S.R.K., D.O.S., and A.W.; supervision, A.W.

DECLARATION OF INTERESTS

The authors declare no competing interests.

Received: January 18, 2024
Revised: April 9, 2024
Accepted: May 7, 2024
Published: June 3, 2024

REFERENCES

1. Mavlonov, A., Razykov, T., Raziq, F., Gan, J., Chantana, J., Kawano, Y., Nishimura, T., Wei, H., Zakutayev, A., Minemoto, T., et al. (2020). A review of Sb_2Se_3 photovoltaic absorber materials and thin-film solar cells. Sol. Energy *201*, 227–246. https://doi.org/10.1016/j.solener.2020.03.009.
2. Bindu, K., Nair, M.T.S., and Nair, P.K. (2006). Chemically deposited Se thin films and their use as a planar source of selenium for the formation of metal selenide layers. J. Electrochem. Soc. *153*, C526. https://doi.org/10.1149/1.2201471.
3. Messina, S., Nair, M.T.S., and Nair, P.K. (2009). Antimony selenide absorber thin films in all-chemically deposited solar cells. J. Electrochem. Soc. *156*, H327. https://doi.org/10.1149/1.3089358.
4. Zhao, Y., Wang, S., Li, C., Che, B., Chen, X., Chen, H., Tang, R., Wang, X., Chen, G., Wang, T., et al. (2022). Regulating deposition kinetics via a novel additive-assisted chemical bath deposition technology enables fabrication of 10.57%-efficiency Sb_2Se_3 solar cells. Energy Environ. Sci. *15*, 5118–5128. https://doi.org/10.1039/D2EE02261C.
5. Shockley, W., and Queisser, H.J. (1961). Detailed balance limit of efficiency of p-n junction solar cells. J. Appl. Phys. *32*, 510–519. https://doi.org/10.1063/1.1736034.
6. Chen, C., and Tang, J. (2020). Open-circuit voltage loss of antimony chalcogenide solar cells: status, origin, and possible solutions. ACS Energy Lett. *5*, 2294–2304. https://doi.org/10.1021/acsenergylett.0c00940.
7. Nayak, P.K., Mahesh, S., Snaith, H.J., and Cahen, D. (2019). Photovoltaic solar cell technologies: analysing the state of the art. Nat. Rev. Mater. *4*, 269–285. https://doi.org/10.1038/s41578-019-0097-0.
8. Choi, Y.C., Mandal, T.N., Yang, W.S., Lee, Y.H., Im, S.H., Noh, J.H., and Seok, S.I. (2014). Sb_2Se_3-Sensitized Inorganic–Organic Heterojunction Solar Cells Fabricated Using a Single-Source Precursor. Angew. Chem. Int. Ed. *126*, 1353–1357. https://doi.org/10.1002/ange.201308331.
9. Zhou, Y., Leng, M., Xia, Z., Zhong, J., Song, H., Liu, X., Yang, B., Zhang, J., Chen, J., Zhou, K., et al. (2014). Solution-processed antimony selenide heterojunction solar cells. Adv. Energy Mater. *4*, 1301846. https://doi.org/10.1002/aenm.201301846.

10. Duan, Z., Liang, X., Feng, Y., Ma, H., Liang, B., Wang, Y., Luo, S., Wang, S., Schropp, R.E., Mai, Y., et al. (2022). Sb_2Se_3 Thin-Film Solar Cells Exceeding 10% Power Conversion Efficiency Enabled by Injection Vapor Deposition Technology. Adv. Mater. *34*, 2202969. https://doi.org/10.1002/adma.202202969.

11. Zhou, Y., Wang, L., Chen, S., Qin, S., Liu, X., Chen, J., Xue, D.-J., Luo, M., Cao, Y., Cheng, Y., et al. (2015). Thin-film Sb_2Se_3 photovoltaics with oriented one-dimensional ribbons and benign grain boundaries. Nat. Photonics *9*, 409–415. https://doi.org/10.1038/nphoton.2015.78.

12. Li, D.-B., Yin, X., Grice, C.R., Guan, L., Song, Z., Wang, C., Chen, C., Li, K., Cimaroli, A.J., Awni, R.A., et al. (2018). Stable and efficient CdS/Sb_2Se_3 solar cells prepared by scalable close space sublimation. Nano Energy *49*, 346–353. https://doi.org/10.1016/j.nanoen.2018.04.044.

13. Wen, X., Chen, C., Lu, S., Li, K., Kondrotas, R., Zhao, Y., Chen, W., Gao, L., Wang, C., Zhang, J., et al. (2018). Vapor transport deposition of antimony selenide thin film solar cells with 7.6% efficiency. Nat. Commun. *9*, 2179. https://doi.org/10.1038/s41467-018-04634-6.

14. Leng, M., Luo, M., Chen, C., Qin, S., Chen, J., Zhong, J., and Tang, J. (2014). Selenization of Sb_2Se_3 absorber layer: an efficient step to improve device performance of CdS/Sb_2Se_3 solar cells. Appl. Phys. Lett. *105*, 083905. https://doi.org/10.1063/1.4894170.

15. Rijal, S., Li, D.-B., Awni, R.A., Bista, S.S., Song, Z., and Yan, Y. (2021). Influence of post-selenization temperature on the performance of substrate-type Sb_2Se_3 solar cells. ACS Appl. Energy Mater. *4*, 4313–4318. https://doi.org/10.1021/acsaem.1c00657.

16. Fleck, N., Hutter, O.S., Phillips, L.J., Shiel, H., Hobson, T.D., Dhanak, V.R., Veal, T.D., Jäckel, F., Durose, K., and Major, J.D. (2020). How oxygen exposure improves the back contact and performance of antimony selenide solar cells. ACS Appl. Mater. Interfaces *12*, 52595–52602. https://doi.org/10.1021/acsami.0c14256.

17. Ren, D., Fu, B., Li, Z., Zhu, B., Li, C., Ji, J., Chen, S., Ma, H., and Zhang, X. (2023). Study of Sb_2Se_3/Al interface affected by oxygen exposure. Vacuum *215*, 112393. https://doi.org/10.1016/j.vacuum.2023.112393.

18. Liu, X., Xiao, X., Yang, Y., Xue, D., Li, D., Chen, C., Lu, S., Gao, L., He, Y., Beard, M.C., et al. (2017). Enhanced Sb_2Se_3 solar cell performance through theory-guided defect control. Prog. Photovolt. *25*, 861–870.

19. Savory, C.N., and Scanlon, D.O. (2019). The complex defect chemistry of antimony selenide. J. Mater. Chem. A *7*, 10739–10744. https://doi.org/10.1039/C9TA02022E.

20. Huang, M., Xu, P., Han, D., Tang, J., and Chen, S. (2019). Complicated and unconventional defect properties of the quasi-one-dimensional photovoltaic semiconductor Sb_2Se_3. ACS Appl. Mater. Interfaces *11*, 15564–15572. https://doi.org/10.1021/acsami.9b01220.

21. Stoliaroff, A., Lecomte, A., Rubel, O., Jobic, S., Zhang, X., Latouche, C., and Rocquefelte, X. (2020). Deciphering the role of key defects in Sb_2Se_3, a promising candidate for chalcogenide-based solar cells. ACS Appl. Energy Mater. *3*, 2496–2509. https://doi.org/10.1021/acsaem.9b02192.

22. Huang, M., Cai, Z., Wang, S., Gong, X.-G., Wei, S.-H., and Chen, S. (2021). More Se vacancies in Sb_2 Se_3 under Se-rich conditions: an abnormal behavior induced by defect-correlation in compensated compound semiconductors. Small *17*, 2102429.

23. Wang, X., Kavanagh, S.R., Scanlon, D.O., and Walsh, A. (2023). Four-electron negative-*U* vacancy defects in antimony selenide. Phys. Rev. B *108*, 134102. https://doi.org/10.1103/PhysRevB.108.134102.

24. Zeng, K., Xue, D.-J., and Tang, J. (2016). Antimony selenide thin-film solar cells. Semicond. Sci. Technol. *31*, 063001. https://doi.org/10.1088/0268-1242/31/6/063001.

25. Tang, R., Zheng, Z.-H., Su, Z.-H., Li, X.-J., Wei, Y.-D., Zhang, X.-H., Fu, Y.-Q., Luo, J.-T., Fan, P., and Liang, G.-X. (2019). Highly efficient and stable planar heterojunction solar cell based on sputtered and post-selenized Sb_2Se_3 thin film. Nano Energy *64*, 103929. https://doi.org/10.1016/j.nanoen.2019.103929.

26. Dou, B., Falletta, S., Neugebauer, J., Freysoldt, C., Zhang, X., and Wei, S.-H. (2023). Chemical trend of nonradiative recombination in Cu(In,Ga)Se_2 alloys. Phys. Rev. Appl. *19*, 054054.

27. Kavanagh, S.R., Walsh, A., and Scanlon, D.O. (2021). Rapid recombination by cadmium vacancies in CdTe. ACS Energy Lett. *6*, 1392–1398. https://doi.org/10.1021/acsenergylett.1c00380.

28. Mosquera-Lois, I., and Kavanagh, S.R. (2021). In search of hidden defects. Matter *4*, 2602–2605. https://doi.org/10.1016/j.matt.2021.06.003.

29. Mosquera-Lois, I., Kavanagh, S.R., Walsh, A., and Scanlon, D.O. (2022). ShakeNbreak: navigating the defect configurational landscape. J. Open Source Softw. *7*, 4817. https://doi.org/10.21105/joss.04817.

30. Mosquera-Lois, I., Kavanagh, S.R., Walsh, A., and Scanlon, D.O. (2023). Identifying the ground state structures of point defects in solids. npj Comput. Mater. *9*, 25. https://doi.org/10.1038/s41524-023-00973-1.

31. Wang, X., Li, Z., Kavanagh, S.R., Ganose, A.M., and Walsh, A. (2022). Lone pair driven anisotropy in antimony chalcogenide semiconductors. Phys. Chem. Chem. Phys. *24*, 7195–7202. https://doi.org/10.1039/d1cp05373f.

32. Goyal, A., Gorai, P., Peng, H., Lany, S., and Stevanović, V. (2017). A computational framework for automation of point defect calculations. Comput. Mater. Sci. *130*, 1–9. https://doi.org/10.1016/j.commatsci.2016.12.040.

33. Kononov, A., Lee, C.-W., Shapera, E.P., and Schleife, A. (2023). Identifying native point defect configurations in α-alumina. J. Phys.: Condens. Matter *35*, 334002. https://doi.org/10.1088/1361-648X/acd3cf.

34. Motti, S.G., Meggiolaro, D., Martani, S., Sorrentino, R., Barker, A.J., De Angelis, F., and Petrozza, A. (2019). Defect activity in lead halide perovskites. Adv. Mater. *31*, e1901183. https://doi.org/10.1002/adma.201901183.

35. Ma, C., Guo, H., Wang, X., Chen, Z., Cang, Q., Jia, X., Li, Y., Yuan, N., and Ding, J. (2019). Fabrication of Sb_2 Se_3 thin film solar cells by co-sputtering of Sb_2Se_3 and Se targets. Sol. Energy *193*, 275–282. https://doi.org/10.1016/j.solener.2019.09.046.

36. Liu, X., Chen, J., Luo, M., Leng, M., Xia, Z., Zhou, Y., Qin, S., Xue, D.-J., Lv, L., Huang, H., et al. (2014). Thermal evaporation and characterization of Sb_2Se_3 thin film for substrate Sb_2 Se_3/CdS solar cells. ACS Appl. Mater. Interfaces *6*, 10687–10695. https://doi.org/10.1021/am502427s.

37. Zhou, Y., Li, Y., Luo, J., Li, D., Liu, X., Chen, C., Song, H., Ma, J., Xue, D.-J., Yang, B., et al. (2017). Buried homojunction in CdS/Sb_2Se_3 thin film photovoltaics generated by interfacial diffusion. Appl. Phys. Lett. *111*, 013901. https://doi.org/10.1063/1.4991539.

38. Kavanagh, S.R., Scanlon, D.O., Walsh, A., and Freysoldt, C. (2022). Impact of metastable defect structures on carrier recombination in solar cells. Faraday Discuss. *239*, 339–356. https://doi.org/10.1039/d2fd00043a.

39. Kim, S., Márquez, J.A., Unold, T., and Walsh, A. (2020). Upper limit to the photovoltaic efficiency of imperfect crystals from first principles. Energy Environ. Sci. *13*, 1481–1491. https://doi.org/10.1039/D0EE00291G.

40. Kim, S., and Walsh, A. (2021). Ab initio calculation of the detailed balance limit to the photovoltaic efficiency of single pn junction kesterite solar cells. Appl. Phys. Lett. *118*, 243905.

41. Li, Z.-Q., Ni, M., and Feng, X.-D. (2020). Simulation of the Sb_2Se_3 solar cell with a hole transport layer. Mater. Res. Express *7*, 016416. https://doi.org/10.1088/2053-1591/ab5fa7.

42. Li, Z., Chen, X., Zhu, H., Chen, J., Guo, Y., Zhang, C., Zhang, W., Niu, X., and Mai, Y. (2017). Sb_2Se_3 thin film solar cells in substrate configuration and the back contact selenization. Sol. Energy Mater. Sol. Cells *161*, 190–196. https://doi.org/10.1016/j.solmat.2016.11.033.

43. Kim, J., Ji, S., Jang, Y., Jeong, G., Choi, J., Kim, D., Nam, S.-W., and Shin, B. (2021). Importance of fine control of Se flux for improving performances of Sb_2Se_3 solar cells prepared by vapor transport deposition. Sol. RRL *5*, 2100327. https://doi.org/10.1002/solr.202100327.

44. Li, K., Chen, C., Lu, S., Wang, C., Wang, S., Lu, Y., and Tang, J. (2019). Orientation engineering in low-dimensional crystal-structural materials via seed screening. Adv. Mater. *31*, e1903914. https://doi.org/10.1002/adma.201903914.

45. Lin, J., Mahmood, A., Chen, G., Ahmad, N., Chen, M., Fan, P., Chen, S., Tang, R., and Liang, G. (2022). Crystallographic orientation control and defect passivation for high-efficient antimony selenide thin-film solar cells. Mater. Today Phys. *27*, 100772. https://doi.org/10.1016/j.mtphys.2022.100772.

46. Li, Z., Liang, X., Li, G., Liu, H., Zhang, H., Guo, J., Chen, J., Shen, K., San, X., Yu, W., et al. (2019). 9.2%-efficient core-shell structured antimony

selenide nanorod array solar cells. Nat. Commun. *10*, 1–9.

47. Yu, L., and Zunger, A. (2012). Identification of potential photovoltaic absorbers based on first-principles spectroscopic screening of materials. Phys. Rev. Lett. *108*, 068701. https://doi.org/10.1103/PhysRevLett.108.068701.

48. Birkett, M., Linhart, W.M., Stoner, J., Phillips, L.J., Durose, K., Alaria, J., Major, J.D., Kudrawiec, R., and Veal, T.D. (2018). Band gap temperature-dependence of close-space sublimation grown Sb_2Se_3 by photo-reflectance. APL Mater. *6*, 084901.

49. Nicolás-Marín, M.M., González-Castillo, J.R., Vigil-Galán, O., and Courel, M. (2022). The state of the art of $Sb_2(S, Se)_3$ thin film solar cells: current progress and future prospect. J. Phys. D: Appl. Phys. *55*, 303001. https://doi.org/10.1088/1361-6463/ac5f32.

50. Crovetto, A. (2024). A phenomenological figure of merit for photovoltaic materials. J. Phys. Energy *6*, 025009. https://doi.org/10.1088/2515-7655/ad2499.

51. Wang, X., Ganose, A.M., Kavanagh, S.R., and Walsh, A. (2022). Band versus polaron: charge transport in antimony chalcogenides. ACS Energy Lett. *7*, 2954–2960. https://doi.org/10.1021/acsenergylett.2c01464.

52. Tiedje, T., Yablonovitch, E., Cody, G.D., and Brooks, B.G. (1984). Limiting efficiency of silicon solar cells. IEEE Trans. Electron Devices *31*, 711–716. https://doi.org/10.1109/T-ED.1984.21594.

53. Zhang, S.B., and Northrup, J.E. (1991). Chemical potential dependence of defect formation energies in GaAs: application to Ga self-diffusion. Phys. Rev. Lett. *67*, 2339–2342. https://doi.org/10.1103/PhysRevLett.67.2339.

54. Freysoldt, C., Grabowski, B., Hickel, T., Neugebauer, J., Kresse, G., Janotti, A., and Van de Walle, C.G. (2014). First-principles calculations for point defects in solids. Rev. Mod. Phys. *86*, 253–305. https://doi.org/10.1103/RevModPhys.86.253.

55. Kumagai, Y., and Oba, F. (2014). Electrostatics-based finite-size corrections for first-principles point defect calculations. Phys. Rev. B *89*, 195205. https://doi.org/10.1103/PhysRevB.89.195205.

56. Walsh, A. (2021). Correcting the corrections for charged defects in crystals. npj Comput. Mater. *7*, 72. https://doi.org/10.1038/s41524-021-00546-0.

57. Oba, F., and Kumagai, Y. (2018). Design and exploration of semiconductors from first principles: a review of recent advances. Appl. Phys. Express *11*, 060101. https://doi.org/10.7567/APEX.11.060101.

58. Squires, A.G., Scanlon, D.O., and Morgan, B.J. (2023). py-sc-fermi: self-consistent fermi energies and defect concentrations from electronic structure calculations. J. Open Source Softw. *8*, 4962. https://doi.org/10.21105/joss.04962.

59. Buckeridge, J. (2019). Equilibrium point defect and charge carrier concentrations in a material determined through calculation of the self-consistent fermi energy. Comput. Phys. Commun. *244*, 329–342. https://doi.org/10.1016/j.cpc.2019.06.017.

60. Alkauskas, A., Yan, Q., and Van de Walle, C.G. (2014). First-principles theory of nonradiative carrier capture via multiphonon emission. Phys. Rev. B *90*, 075202. https://doi.org/10.1103/PhysRevB.90.075202.

61. Stoneham, A.M. (1975). Theory of Defects in Solids (Oxford University Press).

62. Turiansky, M.E., Alkauskas, A., Engel, M., Kresse, G., Wickramaratne, D., Shen, J.-X., Dreyer, C.E., and Van de Walle, C.G. (2021). Nonrad: computing nonradiative capture coefficients from first principles. Comput. Phys. Commun. *267*, 108056. https://doi.org/10.1016/j.cpc.2021.108056.

63. Pässler, R. (1976). Relationships between the nonradiative multiphonon carrier-capture properties of deep charged and neutral centres in semiconductors. Physica Status Solidi (b) *78*, 625–635. https://doi.org/10.1002/pssb.2220780222.

64. Shockley, W., and Read, W.T., Jr. (1952). Statistics of the recombinations of holes and electrons. Phys. Rev. *87*, 835–842. https://doi.org/10.1103/PhysRev.87.835.

65. Hall, R.N. (1952). Electron-hole recombination in germanium. Phys. Rev. *87*, 387. https://doi.org/10.1103/PhysRev.87.387.

66. Alkauskas, A., Dreyer, C.E., Lyons, J.L., and Van de Walle, C.G. (2016). Role of excited states in Shockley-read-hall recombination in wide-band-gap semiconductors. Phys. Rev. B *93*, 201304. https://doi.org/10.1103/PhysRevB.93.201304.

67. Kohn, W., and Sham, L.J. (1965). Self-consistent equations including exchange and correlation effects. Phys. Rev. *140*, A1133–A1138. https://doi.org/10.1103/PhysRev.140.A1133.

68. Dreizler, R.M., and Gross, E.K. (1990). Density functional theory of relativistic systems. In Density Functional Theory (Springer), pp. 245–271.

69. Kresse, G., and Furthmüller, J. (1996). Efficient iterative schemes for ab initio total-energy calculations using a plane-wave basis set. Phys. Rev. B Condens. Matter *54*, 11169–11186. https://doi.org/10.1103/physrevb.54.11169.

70. Kresse, G., and Joubert, D. (1999). From ultrasoft pseudopotentials to the projector augmented-wave method. Phys. Rev. B *59*, 1758–1775. https://doi.org/10.1103/PhysRevB.59.1758.

71. Guo, L., Zhang, B., Ranjit, S., Wall, J., Saurav, S., Hauser, A.J., Xing, G., Li, L., Qian, X., and Yan, F. (2019). Interface engineering via sputtered oxygenated cds: O window layer for highly efficient Sb_2Se_3 thin-film solar cells with efficiency above 7%. Sol. RRL *3*, 1900225. https://doi.org/10.1002/solr.201900225.

72. Guo, L., Zhang, B., Li, S., Montgomery, A., Li, L., Xing, G., Zhang, Q., Qian, X., and Yan, F. (2019). Interfacial engineering of oxygenated chemical bath–deposited cds window layer for highly efficient Sb_2Se_3 thin-film solar cells. Mater. Today Phys. *10*, 100125. https://doi.org/10.1016/j.mtphys.2019.100125.

73. Heyd, J., Scuseria, G.E., and Ernzerhof, M. (2003). Hybrid functionals based on a screened Coulomb potential. J. Chem. Phys. *118*, 8207–8215. https://doi.org/10.1063/1.1564060.

74. Krukau, A.V., Vydrov, O.A., Izmaylov, A.F., and Scuseria, G.E. (2006). Influence of the exchange screening parameter on the performance of screened hybrid functionals. J. Chem. Phys. *125*, 224106. https://doi.org/10.1063/1.2404663.

75. Grimme, S. (2004). Accurate description of van der Waals complexes by density functional theory including empirical corrections. J. Comput. Chem. *25*, 1463–1473. https://doi.org/10.1002/jcc.20078.

76. Filip, M.R., Patrick, C.E., and Giustino, F. (2013). GW quasiparticle band structures of stibnite, antimonselite, bismuthinite, and guanajuatite. Phys. Rev. B *87*, 205125. https://doi.org/10.1103/PhysRevB.87.205125.

77. Kavanagh, S.R., Squires, A.G., Nicolson, A., Mosquera-Lois, I., Ganose, A.M., Zhu, B., Brlec, K., Walsh, A., and Scanlon, D.O. (2024). doped: python toolkit for robust and repeatable charged defect supercell calculations. J. Open Source Softw. *9*, 6433. https://doi.org/10.21105/joss.06433.

78. Luo, X., Ren, D., Zhang, R., Wang, Y., Chen, S., Cathelinaud, M., Xu, Y., Qiao, X., Zhang, X., and Fan, X. (2022). Homogroup Bi/Sb Lattice Substitution to Enhance the Photoelectric Properties of Sb_2Se_3 Crystals. J. Phys. Chem. C *126*, 8913–8921. https://doi.org/10.1021/acs.jpcc.2c01757.

79. Kim, S., Hood, S.N., van Gerwen, P., Whalley, L.D., and Walsh, A. (2020). CarrierCapture.jl: Anharmonic Carrier Capture. J. Open Source Softw. *5*, 2102. https://doi.org/10.21105/joss.02102.